

Effect of interlayer interaction on magnon properties of vdW honeycomb heterostructures

Jun Shan(单俊), Lichuan Zhang(张礼川), Huasu Fu(付华宿), Yuee Xie(谢月娥), Yuriy Mokrousov, and Yuanping Chen(陈元平)

Citation: Chin. Phys. B, 2025, 34 (**8**): 087501. DOI: 10.1088/1674-1056/adce97
http://cpb.iphy.ac.cn; http://iopscience.iop.org/cpb

What follows is a list of articles you may be interested in

Bifurcation of the bound states in the continuum in a dissipative cavity magnonic system

Xinlin Mi(米锌林), Lijun Yan(闫丽君), Bimu Yao(姚碧霖), Shishen Yan(颜世申), Jinwei Rao(饶金威), and Lihui Bai(柏利慧)
Chin. Phys. B, 2025, 34 (**6**): 067508. DOI: 10.1088/1674-1056/add4e4

Magnon behavior in YIG film under microwave excitation investigated by Brillouin light scattering

Guofu Xu(徐国服), Kang An(安康), Wenjun Ma(马文俊), Xiling Li(李喜玲), C. K. Ong, Chi Zhang(张驰), and Guozhi Chai(柴国志)
Chin. Phys. B, 2025, 34 (**6**): 067507. DOI: 10.1088/1674-1056/add24c

Strain-manipulated dispersion characteristics of magnonic crystals with Dzyaloshinskii-Moriya interaction and applications on spin-wave devices

Chuhan Zhou(周楚涵), Xiaotian Jiao(焦晓天), Jiaxi Xu(徐佳熙), Zhaonian Jin(金兆年), Lin Chen(陈琳), and Zhikuo Tao(陶志阔)
Chin. Phys. B, 2025, 34 (**2**): 027501. DOI: 10.1088/1674-1056/ad9892

Alternating spin splitting of electronic and magnon bands in two-dimensional altermagnetic materials

Qian Wang(王乾), Da-Wei Wu(邬大为), Guang-Hua Guo(郭光华), Meng-Qiu Long(龙孟秋), and Yun-Peng Wang(王云鹏)
Chin. Phys. B, 2024, 33 (**9**): 097507. DOI: 10.1088/1674-1056/ad6425

Frequency combs based on magnon-skyrmion interaction in magnetic nanotubes

Tijjani Abdulrazak, Xuejuan Liu(刘雪娟), Zhejunyu Jin(金哲珺雨), Yunshan Cao(曹云姗), and Peng Yan(严鹏)
Chin. Phys. B, 2024, 33 (**8**): 087503. DOI: 10.1088/1674-1056/ad4ff5

Effect of interlayer interaction on magnon properties of vdW honeycomb heterostructures

Jun Shan(单俊)[1,2], Lichuan Zhang(张礼川)[1,2,†], Huasu Fu(付华宿)[1,2], Yuee Xie(谢月娥)[1,2,‡], Yuriy Mokrousov[3,4], and Yuanping Chen(陈元平)[1,2,§]

[1] *School of Physics and Electronic Engineering, Jiangsu University, Zhenjiang* 212013, *China*
[2] *Jiangsu Engineering Research Center on Quantum Perception and Intelligent Detection of Agricultural Information, Zhenjiang* 212013, *China*
[3] *Peter Grünberg Institute and Institute for Advanced Simulation, Forschungszentrum Jülich and JARA, Jülich* 52425, *Germany*
[4] *Institute of Physics, Johannes Gutenberg University Mainz, Mainz* 55099, *Germany*

(Received 9 February 2025; revised manuscript received 5 April 2025; accepted manuscript online 21 April 2025)

Interlayer interactions in bilayer or multilayer electron systems have been studied extensively, and many exotic physical phenomena have been revealed. However, systematic investigations of the impact of interlayer interactions on magnonic physics are very few. Here, we use a van der Waals (vdW) honeycomb heterostructure as a platform to investigate the modulation of magnon properties in honeycomb AA- and AB-stacking heterostructures with ferromagnetic and antiferromagnetic interlayer interactions, including topological phases and thermal Hall conductivity. Our results reveal that interlayer interactions play a crucial role in modulating the magnonic topology and Hall transport properties of magnetic heterostructures, with potential for experimental realization.

Keywords: vdW honeycomb heterostructure, magnon, topological phase transition, thermal Hall effect

PACS: 75.10.–b, 75.30.Ds, 75.40.Gb, 02.40.Pc

DOI: 10.1088/1674-1056/adce97 **CSTR:** 32038.14.CPB.adce97

1. Introduction

As elementary quasiparticle excitations in magnetic materials, magnons show great potential for applications in fields such as spintronics and quantum information processing, playing a key role in frontier technologies such as magnetic storage and quantum computing.[1,2] Magnons can form macroscopic coherent states via quasi-equilibrium Bose–Einstein condensation and are capable of propagating spin information over longer distances compared to spin currents in metals.[3–6] Given the potential applications of magnons in spintronics, research into their topological and transport properties has become a major topic. For instance, in 2010, the thermal Hall effect (THE) of magnons was experimentally observed for the first time in the pyrochlore $Lu_2V_2O_7$, suggesting that magnons can be modulated by a temperature gradient, which stimulated researchers to perform various investigations in this field.[7] Recently, the magnonic topological insulators Cu(1,3-dc),[8–10] CrI_3,[11] $CrSiTe_3$, and $CrGeTe_3$,[12] the triple Dirac magnonic semimetal Cu_3TeO_6,[13,14] giant thermal Hall conductivity in VI_3,[15] and high magnon spin conductivity in two-dimensional (2D) yttrium iron garnet (YIG) thin films have been experimentally observed.[16] In addition, novel magnonic properties related to, for example, magnonic Weyl semimetals,[17,18] the magnon spin Nernst effect,[19] and the magnonic orbital effect[20] have been theoretically investigated. As the magnonic band structure and transport properties have a close relationship, a thorough understanding of band structure, topology, and transport properties is crucial for the future development of spin-wave devices, which can be used in quantum computing, signal processing, communication technologies, sensors, etc.[21–25]

In recent years, in addition to three-dimensional (3D) systems, remarkable progress has been made in the field of 2D magnonics hosted by kagome,[26–28] honeycomb,[29–32] triangular,[33,34] square,[35,36] and Lieb[37,38] lattices, etc. For instance, 2D magnons have been directly observed in ferromagnetic (FM) honeycomb CrI_3 a few atomic layers thick using the Raman scattering method.[39] Theoretically, it is recognized that modulating the magnitude of the Kitaev interaction within the Heisenberg–Kitaev model can lead to gapless or gapped spin liquid states with different magnonic topological properties on the honeycomb lattice.[40–42] Additionally, many works have demonstrated that spin texture and topological phases may be regulated by an external magnetic field.[43–45] Moreover, special magnetic configurations are utilized to induce topological phase transitions and influence transport properties,[27,46] enriching our understanding of these complex systems. However, in 2D systems, apart from manipulating the magnetic field, it is not easy to establish reliable means for modulating the magnonic topology in real ma-

†Corresponding author. E-mail: Lichuan.zhang@ujs.edu.cn
‡Corresponding author. E-mail: yueex@ujs.edu.cn
§Corresponding author. E-mail: chenyp@ujs.edu.cn

© 2025 Chinese Physical Society and IOP Publishing Ltd. All rights, including for text and data mining, AI training, and similar technologies, are reserved.

terials. Furthermore, as the spin lattice often contains a few magnetic atoms, a rich topological phase diagram is difficult to achieve. Therefore, innovative methods for designing novel magnonic structures should be found and introduced.

In 2D electronic systems, interlayer interactions can be utilized to regulate the electronic and topological properties of few-layer materials.[47–49] Significant changes in electronic properties can be observed by changing the stacking order[50,51] or introducing magic angles,[52–55] such as twisted graphene[56] and CrI_3.[57] Furthermore, by tuning the strength of the interlayer interactions, topological phase transitions can be obtained, which have been predicted in ternary transition-metal chalcogenides $MM'Te_4$ (M = Nb, Ta and M' = Ir, Rh),[50] metal–organic topological insulator bilayers MC_4S_4 (M = Ni and Pt),[58] few-layer phosphorenes,[59] etc. These findings indicate that the modulation of interlayer interactions opens a new path for achieving 2D materials with novel electronic properties, suggesting that the interlayer interaction can be utilized to modulate the magnonic properties in few-layer spin systems. Although it is reported that a variety of topological phases can be obtained in homojunction honeycomb lattice by electron or hole doping in a toy model,[60] there is almost no discussion of the influence of interlayer interaction on the magnonic properties.

In pursuit of a deeper understanding of magnonic heterojunctions, we have developed a theoretical model based on a 2D honeycomb lattice complemented by an effective Hamiltonian. The Hamiltonian includes both first and second-nearest-neighbor (1st and 2nd NN) Heisenberg exchange interactions, in addition to the Dzyaloshinskii–Moriya interaction (DMI). Using linear spin wave theory, we analyze the impact of interlayer interactions and stacking order on the topological properties of magnons. The structure of this paper is as follows: we begin by introducing the computational methods employed, including linear spin-wave theory and magnonic topological theory. We then explore the impact of interlayer interactions on magnon topology and investigate the valley asymmetry phenomenon within FM AA-stacking and AB-stacking. Building on this foundation, we conduct a detailed analysis of the interplay between the magnon topology and THE under AB-stacking. Additionally, we extend this investigation to antiferromagnetic (AFM) AB-stacking. In the concluding section, we summarize our findings and discuss their prospective implications for the design of future magnonic devices.

2. The model and the method

The spin interactions in the 2D honeycomb heterostructure lattice are described using an effective Heisenberg spin Hamiltonian of the following form:

$$H = -\sum_{\langle i,j\rangle,l} J^l_{ij}\boldsymbol{S}^l_i\cdot\boldsymbol{S}^l_j+\sum_{\langle i,j\rangle,l}\boldsymbol{D}^l_{ij}\cdot(\boldsymbol{S}^l_i\times\boldsymbol{S}^l_j) - \sum_{\langle l,l'\rangle,\langle i,j\rangle} J_{c1}\boldsymbol{S}^l_i\cdot\boldsymbol{S}^{l'}_j-\sum_{\langle l,l'\rangle,\langle i,j\rangle} J_{c2}\boldsymbol{S}^l_i\cdot\boldsymbol{S}^{l'}_j, \quad (1)$$

where l and l' index two different layers, J^l_{ij} describes the intralayer Heisenberg exchange interaction between spins $\boldsymbol{S}^l_i$ and $\boldsymbol{S}^l_j$ on sites i and j of layer l, respectively. The 1st and 2nd NN interactions in the l-th layer are labeled as J^l_1 and J^l_2, respectively (see Fig. 1). The second term is derived from the 2nd NN DMI. Here, the vector $\boldsymbol{D}^l_{ij}$ can be expressed as $\boldsymbol{D}^l_{ij}=D_l v_{ij}\boldsymbol{z}$, where $v_{ij}=-v_{ji}=+1$ and -1 based on Moriya's rule for the clockwise and anti-clockwise directions, respectively. Previous theoretical and experimental studies[12,61,62] have established that the DMI contributes to the topological Chern magnon bands in a 2D honeycomb lattice, leading to a nontrivial THE. The interlayer Heisenberg exchange interactions are included in the third and fourth terms of the Hamiltonian, corresponding to the 1st and 2nd NN interlayer couplings, denoted by J_{c1} and J_{c2}, respectively. The nature of interlayer FM or AFM stacking is determined by the signs and magnitudes of J_{c1} and J_{c2}. For simplicity, we fix both J_{c1} and J_{c2} as either negative or positive to represent interlayer FM or AFM coupling, respectively. It should be noted that the single-ion magnetic anisotropy energy (MAE) is neglected in our model, as its magnitude is typically small, and the primary focus of this work is to explore how interlayer exchange interactions influence magnonic topological properties. Further discussion of the impact of MAE is provided in the supplementary information.

The linear spin-wave theory[63,64] is utilized to investigate the properties of magnons. The spin operators $\boldsymbol{S}^l_i$ and $\boldsymbol{S}^l_j$ are replaced by the creation and annihilation operators $a^\dagger_i$ and a_i in Eq. (1) based on the standard Holstein–Primakoff (HP) transformation $S^+_i=\sqrt{2S-a^\dagger_i a_i}\,a_i$, $S^-_i=a^\dagger_i\sqrt{2S-a^\dagger_i a_i}$, $S^z_i=S-a^\dagger_i a_i$. By keeping the second-order terms of $a^\dagger_i$ and a_i and adopting the lattice Fourier transformation, we can thus rewrite the Hamiltonian in the momentum space (denoted by $\boldsymbol{H}_2(\boldsymbol{k})$, where $\boldsymbol{H}_2$ is a $2n\times 2n$ matrix with $n=4$), which represents the number of spins in the unit cell. $\boldsymbol{H}_2$ can be diagonalized using the commutation relation $\mathrm{i}\frac{\mathrm{d}\Phi(\boldsymbol{k})}{\mathrm{d}t}=[\Phi(\boldsymbol{k}),H_2(\boldsymbol{k})]=D\Phi(\boldsymbol{k})$, where the dynamical matrix $D=\hat{g}H_2$. Here, the matrix $\hat{g}$, defined as $\hat{g}=\sigma_z\otimes\mathbb{1}$, $\mathbb{1}$ is an $n\times n$ identity matrix, and the basis of the system is $\Phi(\boldsymbol{k})=[a_{1k},a_{2k},a_{3k},a_{4k},a^\dagger_{1-k},a^\dagger_{2-k},a^\dagger_{3-k},a^\dagger_{4-k}]^{\mathrm{T}}$. In this work, only positive real eigenvalues of D are considered, which correspond to the magnon excitation spectrum in the system.

The magnon Berry curvature is employed to investigate the topological properties of the model in Fig. 1. Here, the magnon Berry curvature of the nth spin-wave branch $\Omega^{xy}_{n\boldsymbol{k}}$ can be expressed as

$$\Omega^{xy}_{n\boldsymbol{k}}=-2\mathrm{Im}\sum_{m\neq n}\frac{\langle\Psi_{n\boldsymbol{k}}|\frac{\partial D(\boldsymbol{k})}{\partial k_x}|\Psi_{m\boldsymbol{k}}\rangle\langle\Psi_{m\boldsymbol{k}}|\frac{\partial D(\boldsymbol{k})}{\partial k_y}|\Psi_{n\boldsymbol{k}}\rangle}{(\varepsilon_{n\boldsymbol{k}}-\varepsilon_{m\boldsymbol{k}})^2}, \quad (2)$$

where $|\Psi_{n\boldsymbol{k}}$ is the right eigenvector corresponding to the eigenvalue $\varepsilon_{n\boldsymbol{k}}$ of the spin-wave Hamiltonian.

To quantitatively characterize the magnonic topology, we introduce the Chern number as a topological invariant in the first Brillouin zone (BZ) for the nth magnon branch, which is given by $C_n = \frac{1}{2\pi}\int \Omega^{xy}_{n\boldsymbol{k}}\,\mathrm{d}\boldsymbol{k}$. Although the Chern number is typically used to describe discrete bands, here we employ an energy criterion of 0.0001 meV to calculate the Chern numbers of bands that exhibit crossing points. The topological THE of magnons is generated by introducing a transverse thermal current under an applied longitudinal temperature gradient. Based on Eq. (2), the transverse thermal Hall conductivity κ^{xy} is written as

$$\kappa^{xy} = -\frac{k_{\mathrm{B}}^2 T}{(2\pi)^2\hbar}\sum_n \int_{\mathrm{BZ}} c_2\left(n_{\mathrm{B}}\left(\varepsilon_{n\boldsymbol{k}}\right)\right)\Omega^{xy}_{n\boldsymbol{k}}\,\mathrm{d}\boldsymbol{k}, \tag{3}$$

where $c_2(\tau) = (1+\tau)\ln^2[(1+\tau)/\tau] - \ln^2\tau - 2\mathrm{Li}_2(-\tau)$, Li_2 represents the dilogarithm function, and $n_{\mathrm{B}}(\varepsilon_{n\boldsymbol{k}}) = (\mathrm{e}^{\varepsilon_{n\boldsymbol{k}}/k_{\mathrm{B}}T} - 1)^{-1}$ is the Bose–Einstein distribution function. Here, we compute $\kappa^{xy}_{\mathrm{lim}}$ at $T = 300$ K as an estimate of the order of magnitude of the effect, although this value lies outside the validity region of our approach.

3. Result

As shown in Figs. 1(a) and 1(b), in a single-layer honeycomb lattice, there are two atoms per unit cell connected by three 1st NN and six 2nd NN Heisenberg exchange interactions, corresponding to one acoustic and one optical branch. Different strengths of the exchange interactions and the DMI result in different bandwidths and bandgaps of magnons. In magnetic insulators or semiconductors, the exchange interaction usually decays rapidly with distance. Therefore, the 2nd-NN interaction is set to 10% of the 1st NN interaction ($J_2^l = 0.1J_1^l$) in the Hamiltonian presented in Eq. (1), which is similar to some 2D FM honeycomb systems, e.g., CrI_3 [11,65] and $CrGeTe_3$.[12,61,65] In addition, to simplify the calculation, we restrict the magnitudes of the exchange interaction and DMI for the upper and lower layers in the heterostructure by the relations $D_1 = 2D_2$ and $J^1_{ij} = 2J^2_{ij}$, which resemble the cases of magnetic $CrGeTe_3$ and $CrSiTe_3$.[12,61] For concreteness, the parameters in our model are selected as follows: $J_1^1 = -3$ meV, $J_2^1 = -0.3$ meV, $J_1^2 = -1.5$ meV, $J_2^2 = -0.15$ meV, $D_1 = -0.2$ meV, and $D_2 = -0.1$ meV. The heterostructure is engineered by aligning two distinct monolayers in an appropriate stacking order. We refer to the two stacking orders as AA and AB. As shown in Fig. 1(c), one layer is positioned directly above the corresponding atoms in the adjacent layer, forming AA-stacking. When atoms from one layer are positioned above the unoccupied regions of the other layer, as shown in Fig. 1(d), we realize AB-stacking, which is analogous to the Bernal stacking of graphene.[66–69]

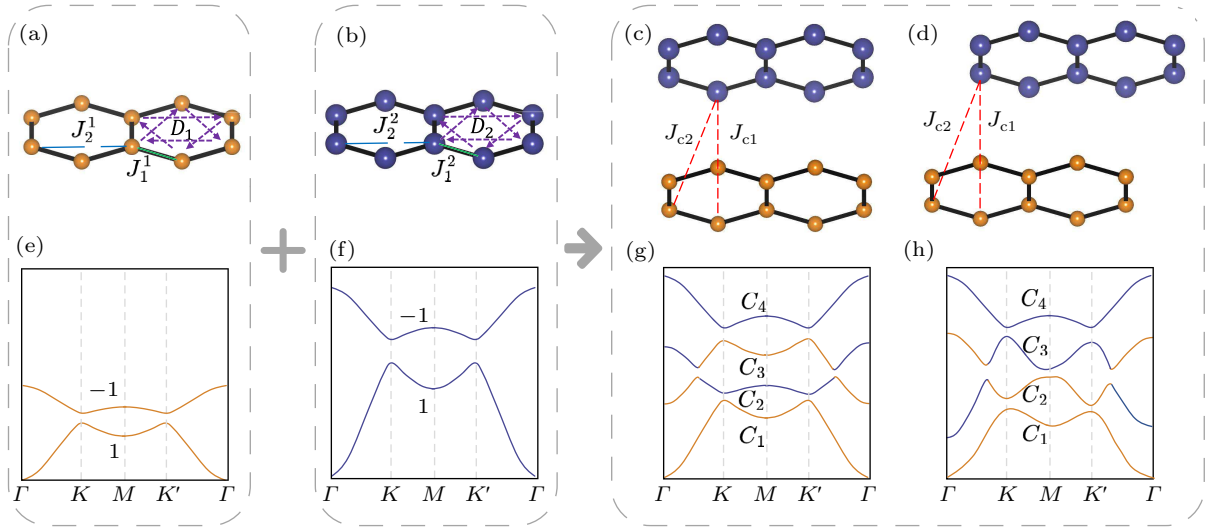


Fig. 1. Schematics and structures. In panels (a) and (b), the yellow and blue atoms represent different 2D FM honeycomb lattices. The 1st and 2nd NN intralayer exchange interactions are represented by blue and green dashed lines, respectively. The purple arrows represent the bond directions of the DMIs between the 2nd NN atoms, and all the Dzyaloshinskii–Moriya vectors share a common sign along the c-axis. The red dashed lines in panels (c) and (d) represent the 1st and 2nd NN interlayer interactions. (e)–(h) The schematic magnonic band structures of panels (a)–(d). In (g) and (h), the yellow and purple bands represent the contributions from the lower layer and the upper layer, respectively. Bandgaps appear between the bands at the K and K' points as well as along the G–K (K') path.

3.1. Topological properties of FM AB-stacking

In the FM type of AA-stacking, there are one 1st NN J_{c1} and three 2nd NN J_{c2} interlayer interactions between the two layers. To investigate the effect of the interlayer interactions on the magnonic properties, the interlayer interactions J_{c1} and J_{c2} are set to values ranging from −3 meV to 0 meV. Specifically, we chose $J_{c1} = 2J_{c2}$ for our study and selected four specific sets of (J_{c1}, J_{c2}) values: (0, 0), (−0.8, −0.4), (−1.6, −0.8), and (−2.5, −1.25). The band structure and the corresponding Chern numbers (C_1, C_2, C_3, C_4) are shown in Fig. 2. In the absence of interlayer interactions, the bands of

the upper and lower layers cross, forming six Dirac points, as shown in detail in Fig. S2. When interlayer interactions are introduced, the band structure shifts up, and the band gap opens between the second and third bands, which causes a topological phase transition with Chern numbers (1, −1, 1, −1). As the interlayer interactions increase, the width of the bands increases and the effect on the bandgap diminishes; as no bandgap closure is observed, the topological phase remains unchanged. This result appears somewhat mundane, as illustrated in Figs. 1(g) and 2. Therefore, we further investigate the case of AB-stacking. With further symmetry reduction, the change of interlayer interactions is likely to trigger more diversity in topological phase transitions.

In AB-stacking, there are one 1st NN J_{c1} and six 2nd NN J_{c2} interlayer interactions, as depicted in Fig. 1(d). To fulfill the FM condition in AB-stacking, we first restrict the parameters J_{c1} and J_{c2} to the range from −3 meV to 0 meV, for which the topological phase diagrams of AB-stacking are presented in Fig. 2(a). To clearly demonstrate the overall characteristics of the Berry curvature of BZ, a logarithmic transformation of the $\Omega^{xy}_{n\boldsymbol{k}}$ is used, which is defined as result = $\mathrm{sgn}(x)\log_{5000}(|x|)$, where the function $\mathrm{sgn}(x)$ refers to the sign of x.

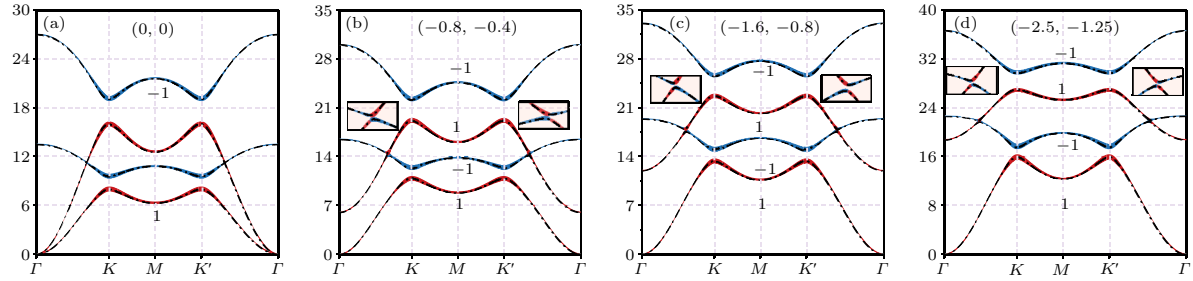


Fig. 2. The case of AA-stacking. (a)–(d) Fat band analysis for the magnonic bands in AA-stacking for different values of J_{c1} and J_{c2}. Red and blue colors represent positive and negative signs of Berry curvature, and the line thickness denotes the corresponding magnitude. The Berry curvature is labeled on a logarithmic scale.

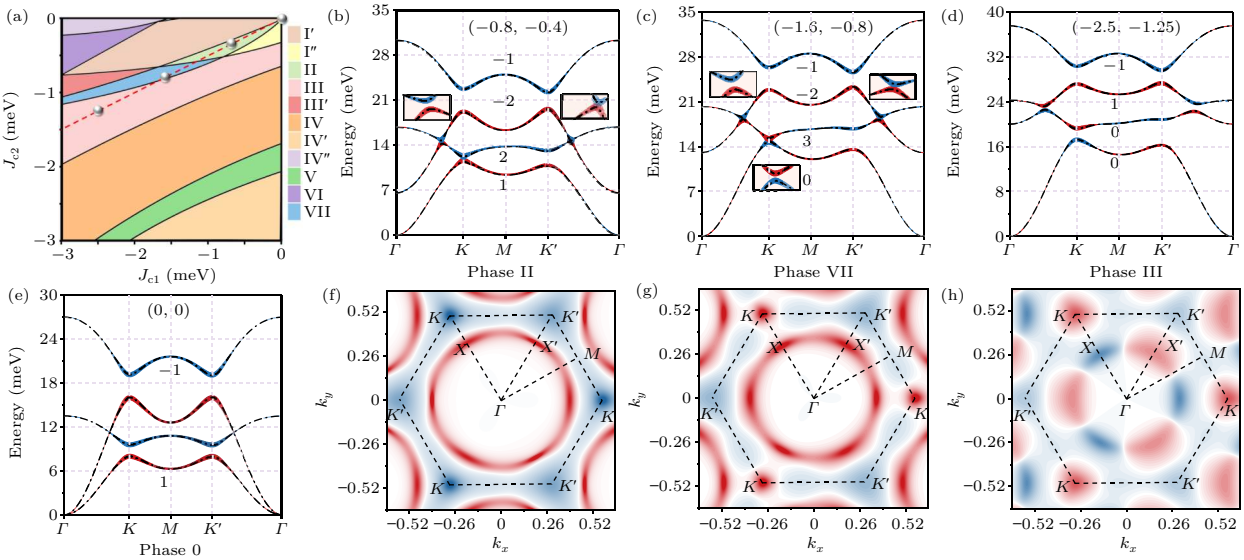


Fig. 3. The case of FM AB-stacking. (a) Topological phase diagram for various interlayer interactions J_{c1} and J_{c2}. (b)–(e) The red dashed line represents $J_{c1} = 2J_{c2}$. Fat band analysis for the magnonic bands in AB-stacking with different values of J_{c1} and J_{c2}. Red and blue colors represent positive and negative signs of Berry curvature, and the line thickness denotes the corresponding magnitude. (f)–(h) The distribution of the k-dependent Berry curvature of the second band in the BZ; parameters are chosen to be the same as those in panels (b)–(d), respectively. All figures in panels (f)–(h) share the same color map. The Berry curvature is labeled on a logarithmic scale.

As with AA-stacking, six Dirac points exist between the second and third bands in the absence of interlayer interactions, as shown in Figs. 3(e) and S4(a). The presence and strength of interlayer interactions can greatly affect the band structure and topological phases. According to the Chern numbers of the four bands (C_1, C_2, C_3, C_4), different phases are observed for various values of J_{c1} and J_{c2}, as shown in Fig. 3(a). In total, there are 11 phases, and we provide a more detailed discussion in supplementary note 3.

To explore the mechanism of phase transition modulated by interlayer interactions, four pairs of (J_{c1}, J_{c2}) along $J_{c1} = 2\ J_{c2}$ are individually chosen, namely, (0, 0), (−0.8, −0.4), (−1.6, −0.8), and (−2.5, −1.25). The corresponding band structures and marked Chern numbers are presented in Figs. 3(b)–3(d), where the Chern numbers (1, 2, −2, −1), (0, 3, −2, −1), and (0, 0, 1, −1) correspond to phases II, VII,

and III. Compared to Figs. 3(b) and 3(e), it can be seen that the phases change from phase 0 to phase II, accompanied by a bandgap opening between bands 2 and 3. As J_{c1} and J_{c2} continue to increase, an inversion between the first and second bands occurs at the K point, resulting in a transition from phase II to phase VII. Further increases in J_{c1} and J_{c2} cause an inversion between the second and third bands, leading to a transition from phase VII to phase III. The Berry curvature projections onto the second band for phases II, VII, and III are shown in Figs. 3(f)–3(h), offering a clearer demonstration of this effect. It is worth noting that due to the breaking of C_2 symmetry, AB-stacking exhibits a valley polarization phenomenon, in contrast to AA-stacking. For instance, the bands at the K and K' points exhibit different behaviors under the influence of interlayer interactions. We provide a more detailed discussion of the valley polarization of magnons and the topological phase transitions in supplementary note 4.

It should be noted that, for simplicity, all innerlayer interaction parameters in our model are fixed throughout the main calculations. However, the resulting topological properties may vary if these parameters are modified. To illustrate this, we further analyze the $CrGeTe_3/CrSiTe_3$ heterostructure by incorporating inner-layer exchange parameters extracted from experimental fittings,[12] i.e., $J_1^1 = -2.73$ meV, $J_2^1 = -0.33$ meV, $J_1^2 = -1.49$ meV, $J_2^2 = -0.15$ meV, $D_1 = -0.12$ meV, and $D_2 = -0.32$ meV. Compared to the results shown in Fig. 3, the corresponding phase diagrams based on the $CrGeTe_3/CrSiTe_3$ heterostructure (see Figs. S10 and S11) exhibit consistent trends, particularly in the regime where J_{c1} and J_{c2} are small, which is more representative of realistic van der Waals heterojunctions.

3.2. Magnonic topology-related thermal Hall conductivity of FM AB-stacking

Next, we compute the thermal Hall conductivity κ^{xy} by referring to Eq. (3), which reflects the effect of weighting the Chern numbers through the c_2 function. The interlayer-interaction-dependent κ^{xy} is shown in Figs. 4(a) and 4(b), where the parameters are $J_{c1} = 2J_{c2}$. Regardless of different interlayer interactions, it is clear that the magnitude of κ^{xy} increases when the temperature increases. In addition, at low temperatures, for a given temperature, κ^{xy} gradually decreases when the interlayer interaction is enhanced, while this phenomenon disappears at high temperatures. This effect can be attributed to the fact that κ^{xy} is strongly linked to nontrivial magnons, which require thermal excitation. Therefore, it is crucial to investigate the relationship between the THE and topological properties. The high-temperature limit κ^{xy} is calculated, and the maximum value of κ^{xy} occurs in phase II, while κ^{xy} reaches its minimum in phase III, as shown in Fig. 4(b). These values are consistent with the corresponding Chern number sets. For instance, in phase II, both C_1 and C_2 are positive, while C_1 and C_2 are zero for phase III. We provide a detailed discussion of the influence that the topological phase exerts on κ^{xy} in supplementary note 5.

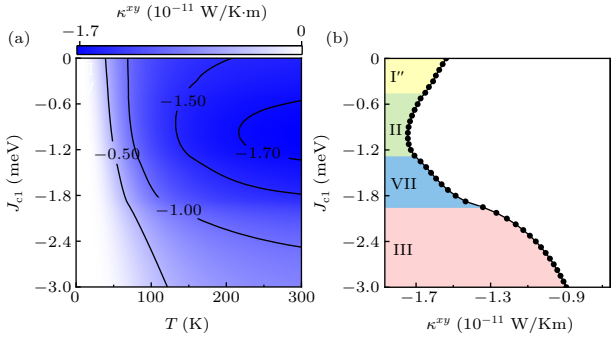


Fig. 4. THE for the FM state of AB-stacking. (a) Map of thermal Hall conductivity κ^{xy} as a function of temperature T and parameter J_{c1}, with $J_{c1} = 2J_{c2}$. (b) Thermal Hall conductivity κ^{xy} as a function of J_{c1} at the high-temperature limit with $J_{c1} = 2J_{c2}$. The corresponding topological phases are marked in different colors.

It is worth noting that in real magnetic systems, the thermal Hall conductivity of magnons is related to the Curie temperature (T_c). Via mean-field theory,[70,71] the T_c values of layer 1 and layer 2 are estimated to be 130.55 K and 65.28 K, respectively (more details are provided in supplementary note 6). Although these T_c values are lower than the high-temperature limit, we believe the characteristic of the maximum κ^{xy} modulated by the interlayer interaction is likely to be similar to the case of the high-temperature limit.

3.3. Topological properties of AFM AB-stacking

In addition to the FM case, we also investigate a magnetic heterojunction with an AFM ground state. As in the case of the FM state, both J_{c1} and J_{c2} are chosen as positive to simplify the analysis. As shown in Fig. 5(a), with the evolution of interlayer interactions, three different topological phases are separately observed in the AFM system, i.e., VIII (1, −1, −1, 1), IX/IX′ (0, 0, −1, 1), and X/X′ (0, 0, 0, 0). Here, IX and IX′ as well as X and X′ are differentiated by their distinct Berry curvature distributions in the BZ. In contrast to the FM case, the magnonic dispersion and topological properties are different in the AFM system. Protected by symmetry, regardless of the interlayer interaction strength, the first and second magnonic branches always remain degenerate at the Γ point, and there is always a crossing point between the second and third branches along the Γ–K/K' lines, as shown in Figs. 5(b) and 5(c) and supplementary note 7.

The Chern number sets and Berry curvature distributions are calculated and shown in Figs. 5(b), 5(c), 5(e), 5(f), S7, and S8, respectively. The results illustrate that the topological phases are modulated by the interlayer interaction, and phase VIII (1, −1, −1, 1) is easily achieved when the interlayer interaction is neglected (see Fig. S7). As the strength of the interlayer interaction increases, there is a transition in the topological phase from phase VIII to phase IX. These phase transi-

tions are characterized by the polarization of magnonic valleys and the alternating closure and reopening of the bandgap between the first and second magnon branches, as depicted in Figs. 4(b), 4(c), and S8.

The thermal Hall conductivity is closely related to the magnonic topology. To simplify the investigation, we set $J_{c1} = 2J_{c2}$ and explore the relationship between κ^{xy} and J_{c1} at different temperatures. As the temperature increases, a reversal of the thermal Hall transport direction is realized. This effect is particularly pronounced when interlayer interactions are weaker than intralayer interactions, as demonstrated in Fig. 4(d). In addition, the high-temperature limit of κ^{xy} for the AFM case is investigated, showing that following the enhancement of interlayer interactions, the magnitude of κ^{xy} first increases and then decreases.

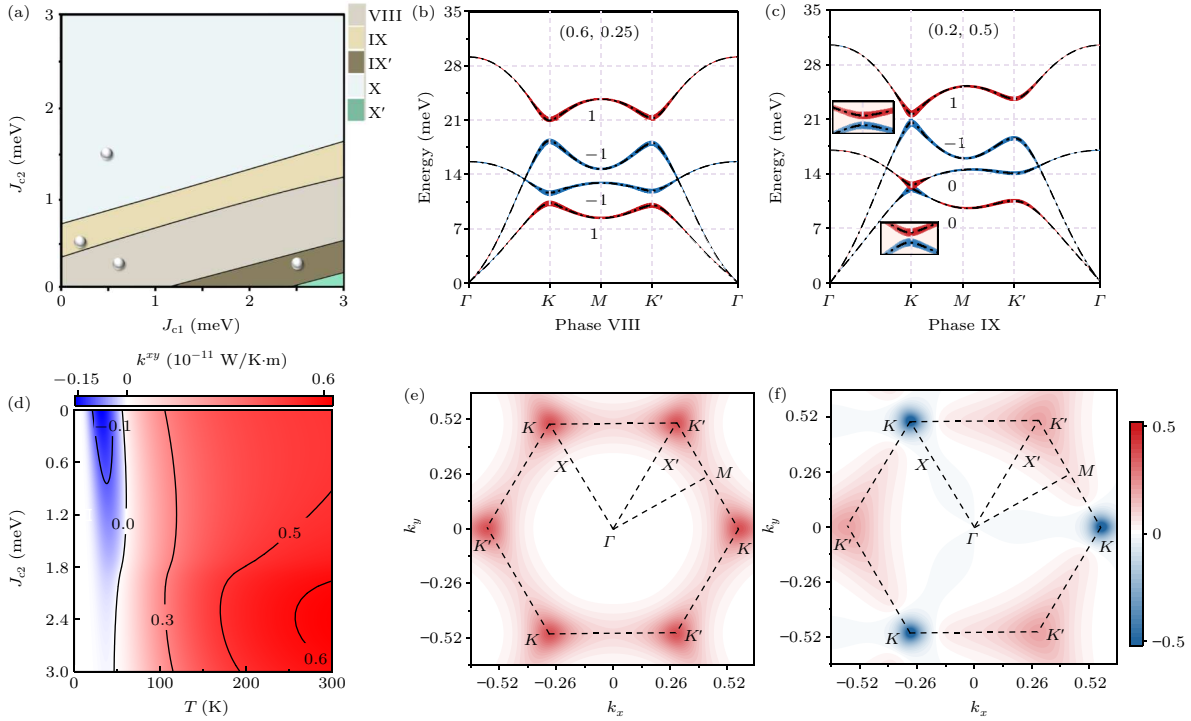


Fig. 5. The case of AFM AB-stacking. (a) Topological phase diagram as a function of J_{c1} and J_{c2} for AFM AB-stacking. (b)–(c) Typical magnonic dispersions for phases VIII (b) and IX (c). (d) Map of κ^{xy} as a function of temperature T and parameter J_{c1} for AFM AB-stacking, with $J_{c1} = 2J_{c2}$. (e) and (f) Distribution of the local Berry curvature in the BZ for the first magnon branch with the same parameters as those used in panels (b) and (c).

4. Conclusions and perspectives

In summary, our work provides a comprehensive theoretical analysis of the impact of interlayer interactions on magnonic topological properties and the THE in van der Waals (VdW) honeycomb heterostructures. Our findings demonstrate that modulating interlayer interactions can significantly alter the magnonic band structure, leading to a diverse range of topological phase transitions and substantial regulation of thermal Hall conductivity, particularly in AB-stacked structures. Additionally, we identify that the magnonic valley polarization phenomenon is especially pronounced in AB-stacked configurations, accompanied by rich topological phases, regardless of whether the magnetic type is FM or AFM.

In the field of magnonics, bilayer spin systems have primarily focused on homojunction configurations.[31,60] Although rich topological phases have been predicted in bilayer honeycomb spin lattices through the introduction of a complex spin Hamiltonian — incorporating interactions such as the Kitaev interaction, DMI, and electron or hole doping — real magnetic systems typically exhibit the Kitaev interaction only in systems with strong spin–orbit coupling and specific structural configurations.[72] In contrast, heterojunctions naturally induce magnonic band crossings and subsequent gap reopenings due to disparities in inner-layer interactions between different layers. This intrinsic mechanism leads to a richer variety of magnonic topological phases and associated transport phenomena, even when a relatively simple effective spin Hamiltonian is employed. It is also worth noting that spin interactions can be easily regulated in layered systems. For example, in bilayer CrI_3, the magnetic type can be modulated from AFM to FM by changing the distance between the two layers.[73] Therefore, our discoveries are not only theoretically significant but also have great potential value for the applications of actual materials. For instance, by constructing heterostructures from $CrXTe_3$ (X = Ge, Si), CrX_3 (X = I, Br, Cl), etc. precise control of magnon properties can be achieved, which is of significant importance for the development of new magnetic storage and quantum computing technologies.

Acknowledgments

Project supported by the National Natural Science Foundation of China (Grant Nos. 12404051, 12347156, 12174157, 12074150, and 12174158), the National Key Research and Development Program of China (Grant No. 2022YFA1405200), the Natural Science Foundation of Jiangsu Province (Grant No. BK20230516), and the Scientific Research Project of Jiangsu University (Grant No. 550171001). Y. M. gratefully acknowledges financial support provided by the Deutsche Forschungsgemeinschaft (DFG, German Research Foundation) – TRR 288/2 – 422213477 (project B06).

References

[1] Bloch F 1930 *Z. Phys.* **61** 206
[2] Majlis N 2007 *The Quantum Theory of Magnetism*
[3] Bozhko D A, Serga A A, Clausen P, Vasyuchka V I, Heussner F, Melkov G A, Pomyalov A, L'vov V S and Hillebrands B 2016 *Nat. Phys.* **12** 1057
[4] Clausen P, Bozhko D A, Vasyuchka V I, Hillebrands B, Melkov G A and Serga A A 2015 *Phys. Rev. B* **91** 220402
[5] Demokritov S O, Demidov V E, Dzyapko O, Melkov G A, Serga A A, Hillebrands B and Slavin A N 2006 *Nature* **443** 430
[6] Kajiwara Y, Harii K, Takahashi S, Ohe J, Uchida K, Mizuguchi M, Umezawa H, Kawai H, Ando K, Takanashi K, Maekawa S and Saitoh E 2010 *Nature* **464** 262
[7] Onose Y, Ideue T, Katsura H, Shiomi Y, Nagaosa N and Tokura Y 2010 *Science* **329** 297
[8] Hirschberger M, Chisnell R, Lee Y S and Ong N P 2015 *Phys. Rev. Lett.* **115** 106603
[9] Li Z D, Zhang R F, Shan J, Alahmed L, Xu A L, Chen Y P, Yuan J R, Cheng X M, Miao X S, Wen J J, Mokrousov Y, Lee Y S, Zhang L C and Li P 2024 *Nano Lett.* **24** 2415
[10] Chisnell R, Helton J S, Freedman D E, Singh D K, Demmel F, Stock C, Nocera D G and Lee Y S 2016 *Phys. Rev. B* **93** 214403
[11] Chen L B, Chung J H, Gao B, Chen T, Stone M B, Kolesnikov A I, Huang Q Z and Dai P C 2018 *Phys. Rev. X* **8**
[12] Zhu F F, Zhang L C, Wang X, dos Santos F J, Song J D, Mueller T, Schmalzl K, Schmidt W F, Ivanov A, Park J T, Xu J H, Ma J, Lounis S, Blügel S, Mokrousov Y, Su Y X and Brückel T 2021 *Sci. Adv.* **7** eabi7532
[13] Bao S, Wang J H, Wang W, Cai Z W, Li S C, Ma Z, Wang D, Ran K J, Dong Z Y, Abernathy D L, Yu S L, Wan X G, Li J X and Wen J S 2018 *Nat. Commun.* **9** 2591
[14] Yao W L, Li C Y, Wang L C, Xue S J, Dan Y, Iida K, Kamazawa K, Li K K, Fang C and Li Y 2018 *Nat. Phys.* **14** 1011
[15] Zhang H D, Xu C Q, Carnahan C, Sretenovic M, Suri N, Di X and Ke X L 2021 *Phys. Rev. Lett.* **127** 247202
[16] Wei X Y, Santos O A, Lusero C H S, Bauer G E W, Ben Youssef J and van Wees B J 2022 *Nat. Mater.* **21** 1352
[17] Li F Y, Li Y D, Kim Y B, Balents L, Yu Y and Chen G 2016 *Nat. Commun.* **7** 12691
[18] Mook A, Henk J and Mertig I 2016 *Phys. Rev. Lett.* **117** 157204
[19] Zyuzin V A and Kovalev A A 2016 *Phys. Rev. Lett.* **117** 217203
[20] Zhang L C, Go D, Hanke J P, Buhl P M, Grytsiuk S, Blügel S, Lux F R and Mokrousov Y 2020 *Commun. Phys.* **3** 227
[21] Wang Q, Chumak A V and Pirro P 2021 *Nat. Commun.* **12** 2636
[22] Pirro P, Vasyuchka V I, Serga A A and Hillebrands B 2021 *Nat. Rev. Mater.* **6** 1114
[23] Chen J, Zhang M, Xu B, Sun J and Mujumdar A S 2020 *Trends Food Sci. Technol.* **105** 251
[24] Yamamoto K, Xu M, Puebla J, Otani Y and Maekawa S 2022 *J. Magn. Magn. Mater.* **545** 168672
[25] Chumak A 2015 *Magnonics view of applications in logic*
[26] Mook A, Henk J and Mertig I 2014 *Phys. Rev. B* **89** 134409
[27] Xing Y H, Chen H, Xu N, Li X and Zhang L F 2022 *Phys. Rev. B* **105** 104409
[28] Mook A, Henk J and Mertig I 2014 *Phys. Rev. B* **90** 0244412
[29] Bai Y X, Zhang L C, Mao N, Li R H, Chen Z Q, Dai Y, Huang B B and Niu C W 2024 *ACS Nano* **18** 13377
[30] Habel J, Mook A, Willsher J and Knolle J 2024 *Phys. Rev. B* **109** 024441
[31] Kim H and Kim S K 2022 *Phys. Rev. B* **106** 104430
[32] Owerre S A 2016 *J. Phys.: Condens. Matter* **28** 436003
[33] Kim H, Saito T, Yang H, Ishizuka H, Coak M J, Lee J H, Sim H, Oh Y S, Nagaosa N and Park J G 2024 *Nat. Commun.* **15** 243
[34] Zhang M H and Yao D X 2023 *Phys. Rev. B* **107** 024408
[35] Zhang M H and Yao D X 2023 *Phys. Rev. B* **108** 144407
[36] Kawano M and Hotta C 2019 *Phys. Rev. B* **99** 054422
[37] Zhuo F J, Kang J, Cheng Z X and Manchon A 2024 *Phys. Rev. B* **109** 054412
[38] Jiang W, Kang M, Huang H Q, Xu H X, Low T and Liu F 2019 *Phys. Rev. B* **99** 125131
[39] Cenker J, Huang B, Suri N, Thijssen P, Miller A, Song T, Taniguchi T, Watanabe K, McGuire M A, Xiao D and Xu X 2021 *Nat. Phys.* **17** 20
[40] Banerjee A, Bridges C A, Yan J Q, Aczel A A, Li L, Stone M B, Granroth G E, Lumsden M D, Yiu Y, Knolle J, Bhattacharjee S, Kovrizhin D L, Moessner R, Tennant D A, Mandrus D G and Nagler S E 2016 *Nat. Mater.* **15** 733
[41] Kasahara Y, Ohnishi T, Mizukami Y, Tanaka O, Ma S, Sugii K, Kurita N, Tanaka H, Nasu J, Motome Y, Shibauchi T and Matsuda Y 2018 *Nature* **559** 227
[42] Kitaev A 2006 *Ann. Phys.* **321** 2
[43] Qi X L, Wu Y S and Zhang S C 2006 *Phys. Rev. B* **74** 085308
[44] Utermohlen F G and Trivedi N 2021 *Phys. Rev. B* **103** 155124
[45] Mochizuki M, Yu X Z, Seki S, Kanazawa N, Koshibae W, Zang J, Mostovoy M, Tokura Y and Nagaosa N 2014 *Nat. Mater.* **13** 241
[46] Chen K, Luo Q, Xi B, Luo H G and Zhao J 2024 *Phys. Rev. B* **109** 174415
[47] Liu S, Wang C, Jeon H, Kim J and Cho J H 2022 *Phys. Rev. B* **105** L041406
[48] He Z, Dou K, Du W, Dai Y, Huang B and Ma Y 2023 *Nano Lett.* **23** 312
[49] Zhao Y, Qiao J, Yu P, Hu Z, Lin Z, Lau S P, Liu Z, Ji W and Chai Y 2016 *Adv. Mater.* **28** 2399
[50] Liu J, Wang H, Fang C, Fu L and Qian X 2017 *Nano Lett.* **17** 467
[51] Zhan D, Yan J X, Lai L F, Ni Z H, Liu L and Shen Z X 2012 *Adv. Mater.* **24** 4055
[52] Qian S, Li Y and Liu C C 2023 *Phys. Rev. B* **108** L241406
[53] Liu Y B, Zhang Y, Chen W and Yang F 2022 *Phys. Rev. B*
[54] Song Z, Wang Z, Shi W, Li G, Fang C and Bernevig B A 2019 *Phys. Rev. Lett.* **123** 036401
[55] Liu B B, Zeng X T, Chen C, Chen Z and Sheng X L 2022 *Phys. Rev. B* **106** 035153
[56] Pathak S, Rakib T, Hou R, Nevidomskyy A, Ertekin E, Johnson H T and Wagner L K 2022 *Phys. Rev. B* **105** 115141
[57] Xu Y, Ray A, Shao Y T, Jiang S, Lee K, Weber D, Goldberger J E, Watanabe K, Taniguchi T, Muller D A, Mak K F and Shan J 2022 *Nat. Nanotechnol.* **17** 143
[58] de Lima F C, Ferreira G J and Miwa R H 2017 *Phys. Rev. B* **96** 115426
[59] Sisakht E T, Fazileh F, Zare M H, Zarenia M and Peeters F M 2016 *Phys. Rev. B* **94** 085417
[60] Ghader D 2021 *New J. Phys.* **23** 053022
[61] Zhang L C, Zhu F, Go D, Lux F R, dos Santos F J, Lounis S, Su Y, Blügel S and Mokrousov Y 2021 *Phys. Rev. B* **103** 134414
[62] Laurell P and Fiete G A 2018 *Phys. Rev. B* **98** 094419
[63] Toth S and Lake B 2015 *J. Phys.: Condens. Matter* **27** 166002
[64] dos Santos F J, dos Santos Dias M, Guimarães F S, Bouaziz J and Lounis S 2018 *Phys. Rev. B* **97** 024431
[65] Xu C, Feng J, Xiang H and Bellaiche L 2018 *npj Comput. Mater.* **4** 57
[66] Zhou H, Holleis L, Saito Y, Cohen L, Huynh W, Patterson C L, Yang F, Taniguchi T, Watanabe K and Young A F 2022 *Science* **375** 774
[67] Kadi F and Malic E 2014 *Phys. Rev. B* **89** 045419
[68] Johansson L I, Armiento R, Avila J, Xia C, Lorcy S, Abrikosov I A, Asensio M C and Virojanadara C 2014 *Sci. Rep.* **4** 4157
[69] de la Barrera S C, Aronson S, Zheng Z, Watanabe K, Taniguchi T, Ma Q, Jarillo-Herrero P and Ashoori R 2022 *Nat. Phys.* **18** 771
[70] Xue Y, Zhang Z, Wu Z and Song C 2022 *J. Appl. Phys.* **132** 053901
[71] Lee I, Utermohlen F G, Weber D, Hwang K, Zhang C, van Tol J, Goldberger J E, Trivedi N and Hammel P C 2020 *Phys. Rev. Lett.* **124** 017201
[72] Takagi H, Takayama T, Jackeli G, Khaliullin G and Nagler S E 2019 *Nat. Rev. Phys.* **1** 264
[73] Soriano D, Cardoso C and Fernández-Rossier J 2019 *Solid State Commun.* **299** 113662